

TECHNISCHE UNIVERSITÄT DORTMUND

PHYSICS DEPARTMENT

INTERNATIONAL MASTER ADVANCED METHODS IN PARTICLE PHYSICS

FACT Experiment

Laboratory report

Date: May 15, 2024

Simone Garnero - simone.garnero@tu-dortmund.de

Bastian Schuchardt - bastian.schuchardt@tu-dortmund.de

Contents

1	Introduction	2
1.1	The FACT experiment	3
1.2	The observation mode	4
1.3	The Crab Nebula	6
2	Dataset	6
3	Acceptance Correction And Calculation Of The Flux	7
4	Unfolding	7
4.1	Naïve SVD Unfolding	8
4.2	Poisson Likelihood Unfolding	8
5	Analysis	8
5.1	Detection Significance	9
5.2	Energy Migration	9
5.3	Unfolding	9
5.4	Acceptance Correction And Calculation Of The Flux	11
5.5	Comparison With MAGIC And HEGRA	11
6	Conclusion	13

The Energy Spectrum of the Crab Nebula Measured with FACT

Advanced Laboratory Course: Particle Physics

Simone Garnero, Bastian Schuchardt

May 15, 2024

Abstract

The objective of this laboratory experiment is to determine the energy spectrum of gamma rays emitted by the Crab Nebula (M1), within the energy range spanning from 500 GeV to 15 TeV. To achieve this, the analysis encompasses data acquired through observations conducted with the Cherenkov telescope FACT, alongside simulated data for the FACT project. Subsequently, the response of the detector to simulated events has been calculated, facilitating the unfolding of measured values to obtain the inherent energy spectrum. Eventually, the results have been compared with the ones obtained by the HEGRA [1] and MAGIC [2] telescopes.

1 Introduction

Gamma-ray astronomy is a crucial component of astroparticle physics, offering a unique perspective on the universe by studying high-energy photons. Together with charged cosmic rays and neutrinos, gamma rays are referred to as *cosmic messengers*. However, unlike the latter two, which are respectively deflected by magnetic fields and very challenging to detect, gamma rays are relatively straightforward to observe, allowing for a clearer understanding of their origins. High-energy photons can be detected either through satellite experiments such as FERMI or indirectly through ground-based Cherenkov telescopes. The utilization of the Cherenkov light emission mechanism has been instrumental in the observation of cosmic gamma-ray sources at very high energies (VHE) for over two decades. Imaging Atmospheric Cherenkov Telescopes (IACTs) [3] have emerged as particularly efficacious tools in this domain, having successfully detected over 100 sources, among which, for example, Supernova Remnants and Active Galactic Nuclei (AGN). The generation of Cherenkov light in the atmosphere, induced by cosmic-ray-induced particle cascades, yields a broad spectrum peaking between 300 nm and 350 nm. These light flashes have a typical photon density at the ground of a few up to several hundred photons per square meter on nano-second time scales. If recorded with an imaging device, the image topology allows to reconstruct energy and direction of the primary particle and to determine its type.



Figure 1: Photograph of the FACT telescope at the Observatorio del Roque de los Muchachos on La Palma (Canary Islands, Spain). The white cylinder visible at the top right is the camera. In the middle of the reflector where one mirror is missing, the light pulser and the video camera are installed. The cooling unit is inside the metal box placed on the telescope platform. [4]

1.1 The FACT experiment

FACT, the **F**irst **G**-APD **C**herenkov **T**elescope [4], is a ground-based imaging atmospheric Cherenkov telescope (IACT). As the name says, it is the first telescope of his kind to use silicon-based sensors for photodetection, situated at the Observatorio del Roque de los Muchachos on La Palma, Canary Islands (Spain). Commencing operations in 2011, it has been remotely controlled since 2012 and has transitioned to robotic operation since 2017. A fundamental objective in the construction of the FACT camera was to validate the suitability of Geiger-mode Avalanche Photodiodes under authentic environmental circumstances. It was imperative to demonstrate that the characteristics of G-APDs remain stable despite their strong dependence on temperature variations and applied voltage. Equally important is the proof that their intrinsic properties, such as their internal crosstalk behavior, do not negatively affect the data quality in Cherenkov telescopes. The FACT experiment, illustrated in Figure 1, consists of several sub-systems serving different purposes during operation. All hardware components are either located on the telescope mount or in a counting room a few meters away. The camera has a total field-of-view of 4.5° and is comprised of 1440 individual pixels equipped with a G-APD and a light concentrator each. All channels are read out individually. The advantage of G-APDs with respect to PMTs is that they offer a high gain

(10^5 to 10^6) and can be operated under much brighter light conditions allowing observations during moon time. Furthermore, their single photon counting capability is a powerful tool for signal calibration, and their compactness and their low operational voltage ($< 100\text{V}$) simplify the camera design. The collection of Cherenkov light is accomplished through the utilization of a sizable reflector, spanning several to a few hundred square meters, which focuses the emitted light onto a rapid and sensitive camera, which exhibits a diameter of 53 cm and extends to a length of 81 cm. It comprises two physically distinct compartments: one designated for housing the photo sensors and another for accommodating the readout electronics. Within the sensor compartment, a plexiglass protection window is incorporated alongside light concentrators positioned at the entrance, with the G-APDs affixed to the rear side of these concentrators. The sensors boast an active area measuring 3×3 mm, evenly subdivided into 3600 cells. This active area is encased within ceramic packaging and safeguarded by a thin (0.3mm) epoxy-resin layer featuring a refractive index ranging between 1.49 and 1.54. This resin layer, with its specified refractive index, establishes a lower cut-off sensitivity threshold around 320 nm for incoming photons, closely aligning with the cut-off introduced by the light concentrators. At room temperature, the dark count rate per sensor is approximately within the range of a few MHz, thus remaining below the night sky background (NSB) rate even during the darkest nights. The G-APDs operate at a gain of $7.5 \cdot 10^5$, exhibiting a peak photon detection efficiency (PDE) of approximately 33% between 450 nm and 500 nm, alongside a crosstalk probability of roughly 13%. This probability denotes the likelihood of a primary avalanche triggering a second or multiple cells. To augment the photo-sensitive area per G-APD, a light concentrator is positioned in front of each sensor. This configuration not only enhances the effective coverage but also addresses issues such as dead space within the packaging and shields against photons originating beyond the reflector surface. A total of 1595 G-APDs were procured for the project. However, to ensure a uniform response across the camera, they were sorted based on their nominal operation voltage, discarding those necessitating excessively low or high voltages. Following this selection process, 1535 sensors remained, operating within a voltage range spanning from 70.64 V to 71.63 V. The employed light concentrators feature a height of 20 mm, a hexagonal entrance with parallel sides separated by a distance of 9.5 mm, and a square exit measuring $2.8 \text{ mm} \times 2.8 \text{ mm}$. The hexagonal shape was chosen to capitalize on its ideal symmetry for the trigger system and event reconstruction purposes.

1.2 The observation mode

Imaging Atmospheric Cherenkov Telescopes (IACTs) often conduct observations utilizing the so-called *wobble mode* [5], wherein the telescope's nominal pointing direction deviates by a certain angle (w , referred to as the wobble distance) from the position of the observed source (or, for extended sources, from its center). The *signal* (or ON) region is integrated within a circular area of angular size θ_c centered around the source, while the *background control* (or OFF) region is similarly defined around a ghost region symmetrically placed with respect to the pointing direction (ensuring equal acceptance). Under such a wobble observation mode, ON and OFF regions are observed simultaneously, optimizing the utilization of the limited duty cycles of IACTs while minimizing potential systematic differences in acceptance for ON and OFF regions. The wobble distance remains fixed during data acquisition. Considering

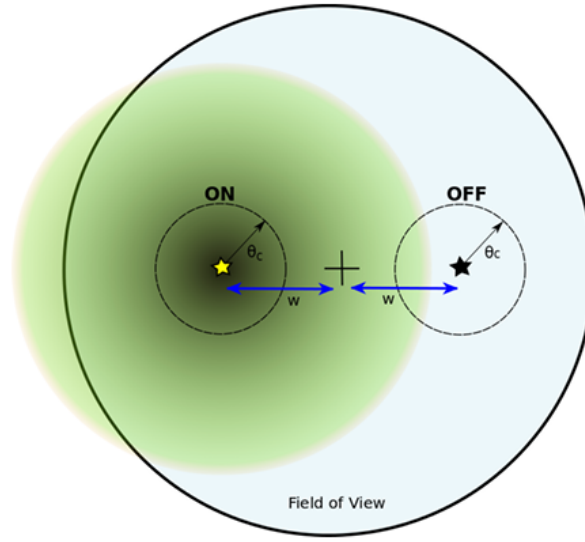


Figure 2: Schematic configuration of the FoV during wobble mode observations. The telescope pointing (black cross) has an offset distance w w.r.t. the center of the source under study (yellow star). ON region is defined as a circle around the center of the source, with angular size θ_c . One background control region (black star) is defined with the same angular size. The leakage effect is schematically shown where, for moderately extended sources (green area), signal events are also expected to be reconstructed inside the OFF region. [6]

that for large values of w , the ON and OFF regions are defined near the edge of the Field of View (FoV), where the instrument's performance diminishes, and for low values of w , defining an appropriate signal-free OFF region may not be feasible, its value should be optimized [6]. In wobble operation mode, a circular ON region of radius θ_c is defined as centered at the source under study (observed at a distance w from the center of the FoV). One or several OFF regions are defined within the same FoV, in such a way that background statistical uncertainties are minimized and instrumental associated uncertainties are also kept low. In Figure 2, a schematic configuration of the FoV during wobble mode observations with only an OFF region is depicted. In the FACT-specific case, the value of w is obtained by an angle of 0.6° and five *background control* regions have been defined, as shown in Figure 3.

The number of reconstructed events in the ON region is denoted as N_{ON} , while in the OFF region, it is represented as N_{OFF} . The significance of the detection can be computed utilizing a likelihood-ratio test, following the method outlined by Li & Ma [7]:

$$S = \sqrt{2} \cdot \sqrt{N_{\text{off}} \ln \left[\frac{1 + \alpha}{\alpha} \left(\frac{N_{\text{off}}}{N_{\text{on}} + N_{\text{off}}} \right) \right] + N_{\text{off}} \ln \left[(1 + \alpha) \left(\frac{N_{\text{off}}}{N_{\text{on}} + N_{\text{off}}} \right) \right]} \quad (1)$$

Where α refers to the size ratio (thus linked to the value θ_c) of the ON region to the OFF regions and, since the OFF regions are five, its value is: $\alpha = 0.2$.

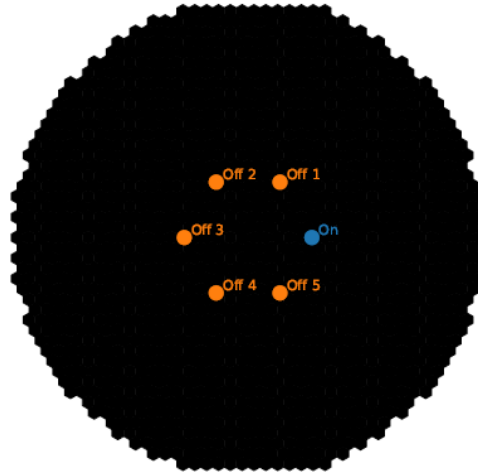


Figure 3: The FACT camera configuration with the ON region and 5 OFF regions

1.3 The Crab Nebula

The Crab pulsar wind nebula (PWN) is a leftover of the supernova explosion that occurred in 1054 A.D., and it is powered by the pulsar PSR B0531+21 at its center [8]. The Crab Nebula is one of the best-studied objects in the sky. Due to its brightness at all wavelengths, precise measurements are provided by different kinds of instruments, allowing for many discoveries, later seen in other non-thermal sources, and a detailed examination of its physics. The Crab Nebula was adopted as a standard candle in many energy regimes, due to its high luminosity and apparent overall long-term flux stability. It has been used to cross-calibrate X-ray and gamma-ray telescopes, to check the instrument performance over time, and to provide units for the emission of other astrophysical objects.

2 Dataset

The dataset available for this analysis consists of three files, containing data from the FACT telescope public repository:

- **open_crab_sample_dl3.hdf5**, containing the reconstructed measurements from 17.7h of observation time of the Crab Nebula
- **gamma_test_dl3.hdf5**, containing the 70% of the simulated response of the FACT telescope
- **gamma_corsika_headers.hdf5**, containing information about all the simulated gamma air showers and the properties of the events generated by the Monte Carlo simulations before reconstruction.

For each air shower event, the reconstructed properties are: the particle class (gamma/hadron), determined through a Random Forest classifier, the energy, estimated using a Random Forest

regressor, only for the gamma candidates, and the direction of origin, reconstructed through a 2D regression using a method called disp-method, either in celestial or detector coordinates.

3 Acceptance Correction And Calculation Of The Flux

The acceptance of a detector is given by the effective area A_{eff} of the detector by

$$A_{\text{eff},i} = \frac{N_{\text{selected},i}}{N_{\text{simulated},i}} \cdot A \quad (2)$$

and must be computed for each bin. The area of the detector is A and has a radius of 270 m. The flux Φ for the unfolded event counts \hat{f} is given by

$$\Phi_i = \frac{\hat{f}_i}{A_{\text{eff},i} \cdot \Delta E_i \cdot t_{\text{obs}}} , \quad (3)$$

where ΔE_i is the bin width and t_{obs} is the observation time of the telescope.

4 Unfolding

In particle physics in general, it is often difficult to measure quantities of interest directly. In astroparticle physics, in particular, indirect measurement methods, which permit obtaining information about a specific quantity by measuring some other, in some way, related quantity, are an everyday occurrence. For example, one can compute the properties of the original particle by measuring the charge deposition in the detector at a specific time. Deducing the underlying distribution of the physical quantity from the distribution of the measurement is a so-called **inverse problem** and can be explicitly described by the Fredholm integral equation:

$$g(y) = \int A(y, x) f(x) dx + b(x) \quad (4)$$

Where, $f(x)$ is the probability density of interest which depends on the physical quantity x , $g(y)$ is the probability density of the measured quantity y , $b(y)$ refers to the background, and $A(y, x)$ is the response function, also known as convolution kernel, which represents the detector and transforms the physical quantity x to the measured quantity y . Since the quantity in which we are interested in a physical experiment is the $f(x)$, Equation (4) must be inverted. In first order, the continuous probability densities can be discretized, so that they correspond to histograms of their respective sizes. In this way, Equation (4) becomes:

$$g = Af + b \quad (5)$$

Where g , b are M vectors, f is an N vector and A is an $N \times M$ matrix. In this case, g is the histogram of the estimated gamma energies for all measured photons, f is the histogram of the true gamma energies, which is the target of the analysis, A the migration matrix of the energy estimators, and b the background histogram derived from the OFF measurements. To complete the unfolding and compute f , it's now necessary to find a good estimator $\hat{f}(g, A, b)$.

There are several unfolding methods; for this analysis, the decision was made to adopt two different unfolding methods and compare the results obtained.

4.1 Naïve SVD Unfolding

The simplest unfolding method is probably the *Naïve SVD* method. It basically consists of computing the inverse matrix of A . Since A is generally an $M \times N$ matrix, one usually considers a generalization of the inverse matrix: the Moore–Penrose inverse matrix A^+ . The acronym SVD in the name of the method stands for *singular value decomposition*. In this case, the estimator is:

$$\hat{f} = A^+(g - b) \quad (6)$$

4.2 Poisson Likelihood Unfolding

This method is based on the assumption that the distribution g is a Poisson distribution. If this is the case, a maximum likelihood fit can be used. The probability of a measured value g_i is given by:

$$P(g_i) = \mathcal{P}(g_i, \lambda_i) \quad (7)$$

with

$$\lambda = A \cdot f + b \quad (8)$$

Hence, the likelihood is:

$$\mathcal{L} = \sum_{i=1}^M \mathcal{P}(g_i, \lambda_i) \quad (9)$$

Considering that numerically it is often preferable to minimize the negative log-likelihood and that the terms that are constant relative to the parameters can be omitted, one obtains:

$$-\ln \mathcal{L} = \sum_{i=1}^M -g_i \cdot \ln \lambda_i + \lambda_i \quad (10)$$

and the estimator in this case becomes:

$$\hat{f} = \arg \min(-\ln \mathcal{L}(f|A, g, b)) \quad (11)$$

5 Analysis

Only the events with confidence of ≥ 0.8 given by the random forest regressor have been chosen to ensure that the events correspond to gamma jets. A theta-square plot of the distance between the assumed and reconstructed source positions to the ON or one of the five OFF positions can be seen in Figure 4. The bins of the histogram for the five OFF positions have been normalized with a factor of $\frac{1}{5}$ to ensure that they can be compared to the ON position. Poisson error was used to compute the uncertainty of the bin heights of the ON positions. Moreover, a selection cut was applied at $\theta^2 \leq 0.025$ to differentiate the signal from the background. This cut will be used through the rest of the analysis.

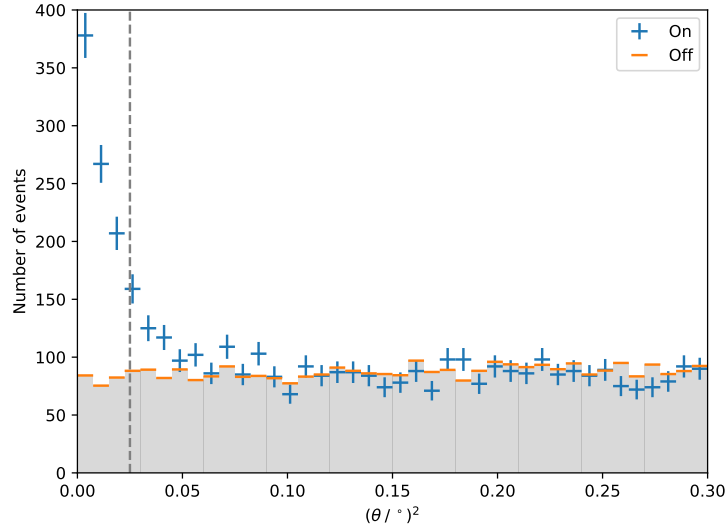


Figure 4: Theta-square plot that shows the difference between the assumed and reconstructed source positions for the ON- and the five OFF-positions. The cut for the data selection can be seen at $\theta^2 \leq 0.025^\circ$.

5.1 Detection Significance

The detection significance S was computed according to Equation Equation 1 to a value of

$$S = 26.28 \pm 1.10, \quad (12)$$

where the Poisson error was assumed for N_{on} and N_{off} to compute the error of the detection significance by error propagation.

5.2 Energy Migration

The energy detector response matrix A was determined by making a two-dimensional histogram of the true and estimated energy of the simulation data according to Equation 5. A heatmap of the matrix can be seen in Figure 5. Logarithmic-equidistant bins between 500 GeV and 15 TeV were chosen with additional underflow and overflow bins. For the true energy, eight bins were used and for the estimated energy 13 bins were used. This was done because inverse problems are better conditioned if the measured quantity has more bins than the quantity that has to be unfolded.

5.3 Unfolding

The naïve SVD and the Poisson likelihood unfolding described in subsection 4.1 and subsection 4.2 were used to unfold the data. The results of both methods can be seen in Figure 6. The background was obtained by putting the five off positions into histograms and normalizing the bin heights by a factor of $\frac{1}{5}$. The y uncertainty was computed by error propagation

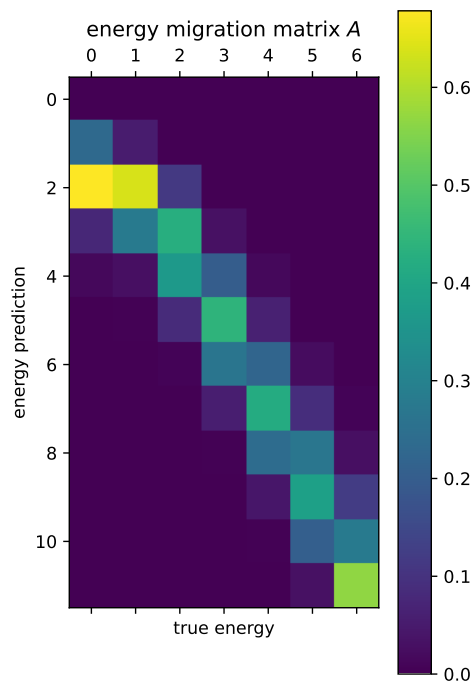


Figure 5: Detector response matrix A . The bins are logarithmic-equidistant spaced and there are one underflow and one overflow bin for the true energy and the estimated energy.

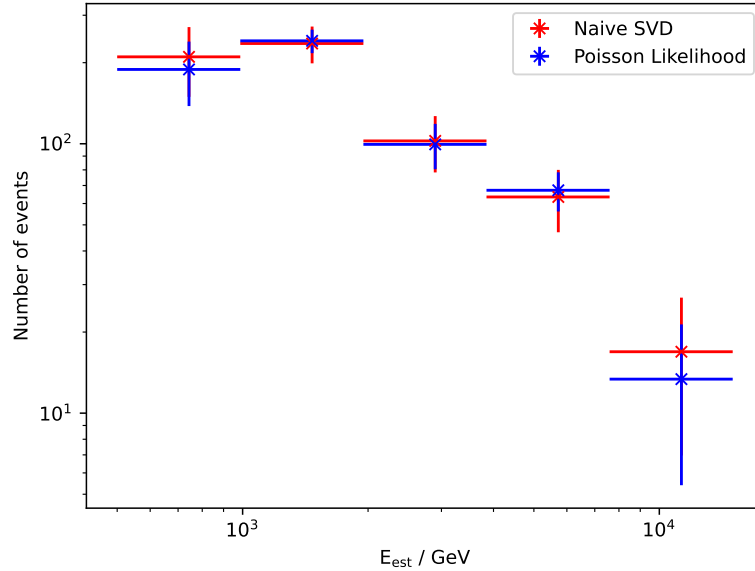


Figure 6: Naïve SVD and Poisson likelihood unfolding for the estimated energy E_{est} in GeV plotted against the number of events. The scale for both axes is logarithmic. The underflow and overflow bins were ignored for the plot.

of the Poisson error of the bin heights. The x uncertainty is the bin width used for the detector response matrix. It can be seen that the Poisson Likelihood unfolding deviates only slightly from the Naïve SVD unfolding for the three bins in the middle and larger deviations can be seen for the two outward bins. The uncertainties of both methods agree.

5.4 Acceptance Correction And Calculation Of The Flux

The calculation of the flux was done according to Equation 1 with an acceptance correction of 70 %, because the dataset only contains this fraction of all the simulated events. The result for both unfolding methods can be seen in Figure 7. Again both unfolding methods have agreeing uncertainties and only small deviations for the first and last bins.

5.5 Comparison With MAGIC And HEGRA

Additionally, a comparison with the spectrum of the crab nebula obtained by the MAGIC and HEGRA telescope can be made. The results can be seen in Figure 8. Overall, the obtained energy spectrum aligns well with power laws given by [2] for the MAGIC telescope and [1] for the HEGRA telescope.

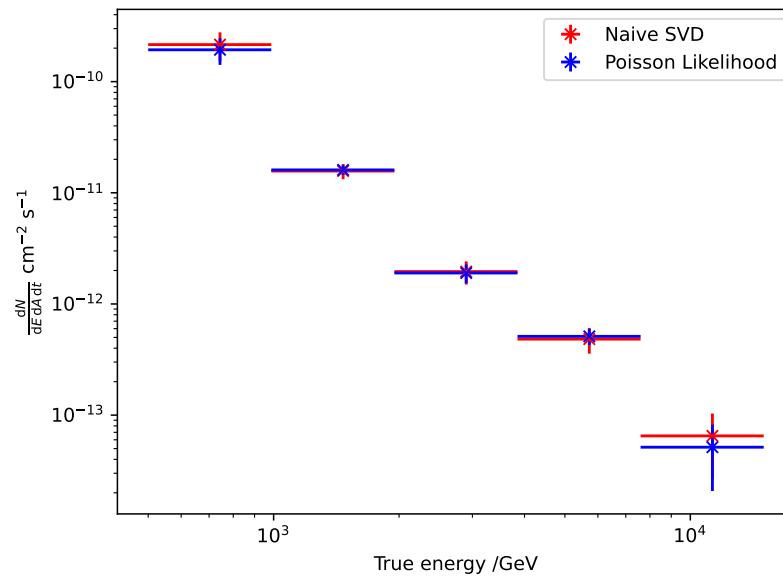


Figure 7: Energy spectrum of the crab nebula in GeV against $\frac{dN}{dE dA dt}$ in $\text{cm}^{-2}\text{s}^{-1}$ for Naïve SVD and Poisson likelihood unfolding.

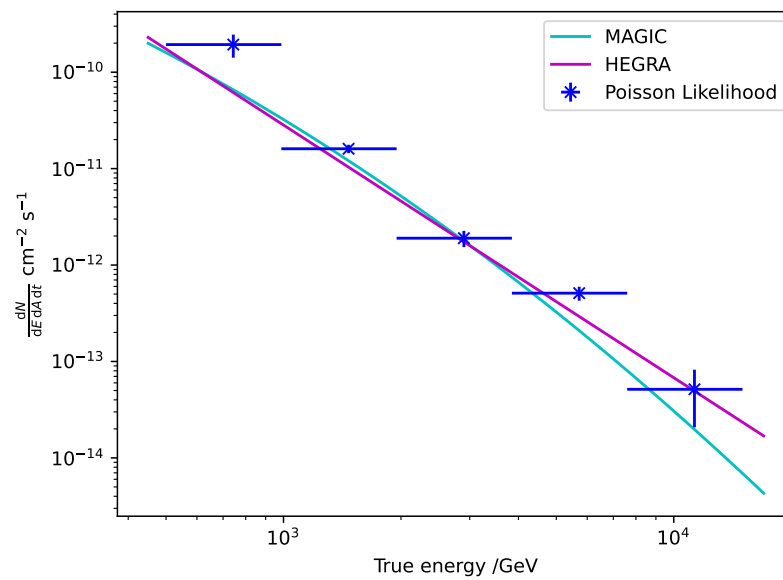


Figure 8: Energy spectrum of the crab nebula in GeV against $\frac{dN}{dE dA dt}$ in $\text{cm}^{-2}\text{s}^{-1}$ for Poisson likelihood and the power laws obtained by MAGIC and HEGRA.

6 Conclusion

Overall, it can be said that the analysis was successful and the result of the energy spectrum of the crab nebula is comparable to the power laws obtained by the MAGIC and HEGRA telescopes. The uncertainties of the results agree with both energy spectrums. The naïve SVD and Poisson likelihood unfolding both yielded similar results.

References

- [1] F. Aharonian et al. The crab nebula and pulsar between 500 gev and 80 tev: Observations with the hegra stereoscopic air cerenkov telescopes. *The Astrophysical Journal*, 614(2):897, oct 2004.
- [2] J. Aleksić et. al. Measurement of the crab nebula spectrum over three decades in energy with the magic telescopes. *Journal of High Energy Astrophysics*, 5–6:30–38, March 2015.
- [3] Adrian Biland, Thomas Bretz, Jens Buß, Volker Commichau, Lubomir Djambazov, Daniela Dorner, Sabrina Einecke, Dorit Eisenacher, Jan Freiwald, Oliver Grimm, et al. Calibration and performance of the photon sensor response of fact—the first g-apd cherenkov telescope. *Journal of Instrumentation*, 9(10):P10012, 2014.
- [4] H Anderhub, Michael Backes, A Biland, Vittorio Boccone, Isabel Braun, Thomas Bretz, J Buß, Franck Cadoux, V Commichau, L Djambazov, et al. Design and operation of fact—the first g-apd cherenkov telescope. *Journal of Instrumentation*, 8(06):P06008, 2013.
- [5] Stefania Gori, Stefano Profumo, and Bibhushan Shakya. Wobbly dark matter signals at cherenkov telescopes from long-lived mediator decays. *Phys. Rev. Lett.*, 122:191103, May 2019.
- [6] J Palacio, D Navarro-Girones, and J Rico. Pointing optimization for iacts on indirect dark matter searches. *Astroparticle Physics*, 104:84–90, 2019.
- [7] T. P. Li and Y. Q. Ma. Analysis methods for results in gamma-ray astronomy. , 272:317–324, September 1983.
- [8] Jelena Aleksić, S Ansoldi, Lucio Angelo Antonelli, P Antoranz, A Babic, P Bangale, JA Barrio, J Becerra González, W Bednarek, Eea Bernardini, et al. Measurement of the crab nebula spectrum over three decades in energy with the magic telescopes. *Journal of High Energy Astrophysics*, 5:30–38, 2015.